separations

MDPI

Article

Understanding the Effects of Inlet Structure on Separation Performance Based on Axial Velocity Wave Zone Characteristics

Shuo Zhang, Baoyu Cui *, Sikai Zhao, Yanbai Shen and Qiang Zhao *

School of Resources and Civil Engineering, Northeastern University, Shenyang 110819, China
* Correspondence: cuibaoyu@mail.neu.edu.cn (B.C.); zhaoqiang@mail.neu.edu.cn (Q.Z.)

Abstract: There are many factors that affect the separation performance of the hydrocyclone, including the structure of the feed body, but the mechanism of influence of the internal flow field of the hydrocyclone on the Axial Velocity Wave Zone (AVWZ) is not yet clear. Based on the numerical test method, this paper analyzes the influence of the feed body structure on the internal flow field and the particle distribution characteristics of the AVWZ and its internal relationship with its separation performance. The results show that the influence mechanism of the structural parameters of the inlet structure on its separation performance is extremely complex, but all of them are reflected in the AVWZ's characteristics, including the flow field characteristics, spatial distribution characteristics, and internal particle distribution. The changes on the inlet diameter will also influence the flow field, centrifugal strength, turbulence strength, and particle distribution, while the inlet aspect ratio is altered largely by changing the settling distance of particles. Finally, effects of inlet structure on the separation performance of the hydrocyclone can be explained from the AVWZ, which provides the basis for designing the inlet structure to improve separation performance.

Keywords: hydrocyclone; axial velocity wave zone; numerical simulation; inlet structure; separation performance

Citation: Zhang, S.; Cui, B.; Zhao, S.; Shen, Y.; Zhao, Q. Understanding the Effects of Inlet Structure on Separation Performance Based on Axial Velocity Wave Zone Characteristics. *Separations* **2023**, *10*, 3. https://doi.org/10.3390/separations10010003

Academic Editor: Jovana Grahovac

Received: 11 November 2022
Revised: 5 December 2022
Accepted: 13 December 2022
Published: 21 December 2022

1. Introduction

The hydrocyclone first appeared in the Netherlands in the late 1930s. It is a device that uses rotary flow for classification, and is also used for concentration, dehydration, and sorting. Since the 1950s, hydrocyclones have been widely and increasingly used in mineral processing plants around the world. At the same time, the research on the internal flow field state of the hydrocyclone was gradually paid more attention, but it was still limited to the mining field. This situation changed fundamentally in the 1980s, and it has since been applied in industrial sectors such as the chemical industry, petroleum, water treatment, and metal processing [1]. A typical hydrocyclone consists of a cylindrical section and a conical section where the central cavity is connected to the discharge pipe. An inlet pipe is connected to the top part of the cylinder. Fluid tangentially injected into a hydrocyclone induces a swirling flow that creates centrifugal force within the device. This centrifugal force field enables the rapid sorting of particulate matter in suspension media. Factors such as inlet velocity, pressure and other operating parameters, inlet structure, and spigot structure will affect the separation performance and efficiency of the hydrocyclone [2,3].

So far, scholars have had a relatively deep understanding of the average flow field characteristics and particle motion of hydrocyclones, but they have not been able to solve two core issues: (1) how to determine the natural separation surface of hydrocyclones; (2) why the hydrocyclone has only a limited separation accuracy. Luo [4], Dai [5], and Liu et al. [6] used LDA (Laser Doppler Anemometry) and PDA (Phase Doppler Anemometry) methods to study the internal flow field of hydrocyclones and found an area near the hydrocyclone LZVV (Locus of zero vertical velocity) in which the axial velocity of each point is close to zero. For the convenience of description, this region is collectively referred

to as the Axial Velocity Wave Zone (AVWZ). According to the research results of Renner and Cohen [7], and the internal axial velocity distribution and particle distribution law of the AVWZ, it is understood that the AVWZ is an extended form of the LZVV in the separation space and its spatial distribution and internal flow field characteristics affect the distribution of medium-sized particles. The separation process affects the separation performance of the hydrocyclone, therefore, the AVWZ is one of the key factors affecting the separation performance of the hydrocyclone. However, the current understanding of the AVWZ is seriously insufficient, and a clear definition for its spatial shape and size has not yet been given. The existing research results only measure the axial velocity in this region, and describe other flow field characteristics such as pressure distribution, turbulent flow distribution, and circulating flow. In addition, the research on the motion behavior and distribution of particles in the AVWZ is mainly limited to the single particle size (or density) particles in the dilute phase, while the motion and distribution of particles with different properties in this region and its underlying mechanisms need to be further studied.

The inlet structure is one of the factors affecting the hydrocyclone's separation performance and many scholars have carried out different research on the structure of the inlet. The current research on the inlet structure is mainly including the size and shape. The size of the inlet structure mainly affects the Euler number and, more precisely, the energy consumption of the hydrocyclone. The first aspect for consideration is the size of the inlet cross-section. At a fixed flow rate, the separation performance can be significantly improved with a decrease in inlet size [8,9]. The second aspect is the cross-sectional shape. According to the literature [10,11], a long and narrow rectangular inlet can slightly improve the separation efficiency compared with a circular inlet of the same cross-sectional area. This is confirmed by comparing the numerical effects of different inlet shapes (circle, ellipse, rectangle, square, and trapezoid), which further proves that this effect is also due to the change in Euler number. The second aspect concerns the shape or profile of the inlet structure. Tangential (or linear) inlets seem to be favored by most manufacturers, but many studies [12,13] have shown that vortex types such as involute, helical, and arcuate inlets can obtain better pre-separation and steering, which helps improve separation efficiency and cuts sharpness, at the cost of higher energy consumption. In contrast, the experimental results of Chu et al. [14] demonstrated that the simplest tangential inlet can achieve higher separation efficiency, cutting sharpness and capacity compared with those of the vortex type under the same inlet pressure conditions.

The two aspects described above have been researched by different scholars who have used different aspects of the inlet structure to study the mechanism of its influence on the separation performance of the hydrocyclone, and provide valuable data for the current research [15]. However, none of the above studies have analyzed the influence and performance of the hydrocyclone from the perspective of the AVWZ. Therefore, this paper does not design a new inlet structure, but further reveals the impact mechanism of the inlet structure on the hydrocyclone's analytical performance from the perspective of the AVWZ. Physical tests and numerical analyses were carried out to analyze the effects of turbulence intensity, tangential velocity, and particle distribution.

2. Establishment of Mathematical Model

2.1. Model Description

2.1.1. Turbulence Model Based on RANS

The turbulence model is a type of differential equation. Commonly used turbulence models can be classified according to the number of differential equations: a zero-equation model, a one-equation model, a two-equation model, a four-equation model, a seven-equation model, etc. [12,16–18].

Although the instantaneous Navier–Stokes equation can describe turbulent flow, the nonlinearity of the equation makes it extremely difficult to obtain an exact solution, and it is rarely used in engineering applications. Unlike DNS (Direct Numerical Simulation) and LES (Large Eddy Simulation), RANS (Reynolds-Averaged Navier–Stokes) does not directly

solve for turbulence at any scale, but instead decomposes the instantaneous velocity into mean and pulsating velocities [19]:

$$u_i = \overline{u}_i + u_i' \tag{1}$$

It should be noted that $\overline{u}_i$ and u_i' here are significantly different from the definitions in LES. After the continuity equation and momentum equation are averaged by the Reynolds-averaging method, the Reynolds stress term $-\rho\overline{u_i'u_j'}$ is introduced, and the turbulent flow model needs to be used to close the averaged Reynolds equations:

$$\frac{\partial \rho}{\partial t} + \frac{\partial}{\partial x_i}(\rho \overline{u}_i) = 0 \tag{2}$$

$$\frac{\partial \rho \overline{u}_i}{\partial t} + \frac{\partial}{\partial x_j}(\rho \overline{u}_i \overline{u}_j) = -\frac{\partial \overline{p}}{\partial x_i} + \frac{\partial}{\partial x_j}\left[\mu\left(\frac{\partial \overline{u}_i}{\partial x_j} + \frac{\partial \overline{u}_j}{\partial x_i}\right)\right] + \frac{\partial}{\partial x_j}\left(-\rho\overline{u_i'u_j'}\right) + \rho g_i + F_i \tag{3}$$

According to different processing methods, RANS turbulence models can be divided into eddy-viscous models and second-order matrix models [20]. Among them, the eddy viscosity model is based on Boussinesq's isotropic eddy viscosity assumption, which is easy to solve [21]. The second-order matrix model directly constructs the Reynolds stress equation, which takes into account the anisotropy, rotation effect, buoyancy effect, and curvature effect of turbulence. Hence, it can describe the complex turbulent motion more accurately. Literature research shows that the fluid flow of the hydrocyclone is a strong rotational shear motion, and the turbulent flow has obvious anisotropy [22]. Only the Reynolds Stress Model (RSM), based on the second-order matrix, can accurately describe the average motion and turbulence intensity. In RSM, the Reynolds stress term $-\rho\overline{u_i'u_j'}$ is solved by the following transport equation:

$$\frac{\partial}{\partial t}\left(\rho\overline{u_i'u_j'}\right) + \frac{\partial}{\partial x_k}\left(\rho u_k \overline{u_i'u_j'}\right) = D_{T,ij} + P_{ij} + G_{ij} + \varphi_{ij} + \varepsilon_{ij} \tag{4}$$

In the formula,

$$\text{Turbulent diffusion term}: \ D_{T,ij} \equiv -\frac{\partial}{\partial x_k}\left[\rho\overline{u_i'u_j'u_k'} + \overline{p'\left(\delta_{kj}u_i' + \delta_{ik}u_j'\right)}\right] \tag{5}$$

$$\text{Stress generating term}: \ P_{ij} \equiv -\rho\left(\overline{u_i'u_k'}\frac{\partial u_j}{\partial x_k} + \overline{u_j'u_k'}\frac{\partial u_i}{\partial x_k}\right) \tag{6}$$

$$\text{Buoyancy generating term}: \ G_{ij} \equiv -\rho\beta\left(g_i\overline{u_j'\theta} + g_j\overline{u_i'\theta}\right) \tag{7}$$

$$\text{Pressure strain term}: \ \varphi_{ij} \equiv p'\left(\frac{\partial u_i'}{\partial x_j} + \frac{\partial u_j'}{\partial x_i}\right) \tag{8}$$

$$\text{Turbulent Dissipation Term}: \ \varepsilon_{ij} \equiv -2\mu\overline{\frac{\partial u_i'}{\partial x_k}\frac{\partial u_j'}{\partial x_k}} \tag{9}$$

Among them, there are two processing methods for the pressure–strain term φ_{ij}, namely, the Linear model and the Quadratic model. For rotational shear flow in hydrocyclones, secondary pressure strain models can provide higher accuracy.

In the RSM, the transport equations for turbulent kinetic energy (k) and turbulent dissipation rate (ε) can be expressed as:

$$\frac{\partial}{\partial t}(\rho k) + \frac{\partial}{\partial x_i}(\rho k u_i) = \frac{\partial}{\partial x_j}\left[\left(\mu + \frac{\mu_t}{\sigma_k}\right)\frac{\partial k}{\partial x_j}\right] + \frac{1}{2}(P_{ii} + G_{ii}) - \rho\varepsilon\left(1 + 2M_t^2\right) \tag{10}$$

$$\frac{\partial}{\partial t}(\rho \varepsilon) + \frac{\partial}{\partial x_i}(\rho \varepsilon u_i) = \frac{\partial}{\partial x_j}\left[\left(\mu + \frac{\mu_t}{\sigma_\varepsilon}\right)\frac{\partial \varepsilon}{\partial x_j}\right] + \frac{1}{2}C_{\varepsilon 1}(P_{ii} + C_{\varepsilon 3}G_{ii})\frac{\varepsilon}{k} - C_{\varepsilon 2}\rho\frac{\varepsilon^2}{k} \tag{11}$$

In the formula, σ_k = 1.0, σ_ε = 1.0, $C_{\varepsilon 1}$ = 1.44, $C_{\varepsilon 2}$ = 1.92, $C_{\varepsilon 3}$ is determined by the direction of flow and gravity, and M_t is the turbulent Mach number.

It should be noted that when the RANS turbulence model is adopted, turbulence is characterized by turbulent intensity, turbulent kinetic energy, and the turbulent dissipation rate, and only a time-homogeneous flow field can be obtained, reflecting the average flow of the fluid.

2.1.2. Gas–Liquid Two-Phase Flow Model

The two-phase model is a numerical model used to simulate the seepage of any two-phase fluid in a porous medium in oil, gas, and water. The key to gas–liquid two-phase flow field simulation is to accurately capture the gas–liquid interface, that is, the position and shape of the air core. According to the literature [23–25], the volume of fluid (VOF) model based on the Eulerian is usually used to simulate the gas–liquid two-phase flow field. The model simulates the flow of two or more immiscible fluids by solving a single momentum equation and tracking the volume fraction of the secondary fluid in the computational domain. For the gas–liquid two-phase flow field of the hydrocyclone, the governing equation is:

$$\frac{\partial \alpha}{\partial t} + \frac{\partial \alpha}{\partial x_i} u_j = 0 \tag{12}$$

$$\frac{\partial \rho u_i}{\partial t} + \frac{\partial}{\partial x_j}\left(\rho u_i u_j\right) = -\frac{\partial p}{\partial x_i} + \frac{\partial}{\partial x_j}\left[\mu\left(\frac{\partial u_i}{\partial x_j} + \frac{\partial u_j}{\partial x_i}\right)\right] + \rho g_i + F_i \tag{13}$$

where α is the air volume fraction with a value in the range [0, 1], ρ and μ are the average density and viscosity of the fluid, the relevant transport equation is written as:

$$\rho = \alpha \rho_{\text{air}} + (1 - \alpha)\rho_{\text{water}} \tag{14}$$

$$\mu = \alpha \mu_{\text{air}} + (1 - \alpha)\mu_{\text{water}} \tag{15}$$

When tracking the gas–liquid interface, the surface tension source term can also be added to the momentum equation to improve the simulation accuracy [26]:

$$F_s = 2\sigma \frac{\rho \kappa \nabla \alpha}{\rho_{\text{water}} \rho_{\text{air}}} \tag{16}$$

where σ represents the surface tension of the gas–liquid interface, and κ is the curvature.

The internal flow field of the hydrocyclone is very complex, especially after adding the particle phase, and it is easy to cause convergence difficulties when solving the gas–liquid–solid multiphase flow directly. Therefore, this paper studies the internal flow field characteristics and separation performance of the AVWZ in two steps. The first step is to adopt the VOF-RSM or the VOF-LES to simulate the gas–liquid two-phase flow field of the hydrocyclone, focusing on the spatial distribution and internal flow field characteristics of the AVWZ. In the second step, on the basis of a stable gas–liquid two-phase flow field, several particle phases are added, and the TFM-RSM or ASM-RSM is used to examine the separation performance of the hydrocyclone and the spatial distribution of particles in the AVWZ.

2.1.3. ASM

The ASM (Algebraic slip model) inherits most of the features of the TFM (Two-Fluid model), such as the particle phase, and is still a continuum that can penetrate each other. The fluid properties of the particle phase are calculated by simplified KTGF (Kinetic Theory for Granular Flow) [27]. In addition, in the ASM, only a set of differential equations need to be solved for the mixed phase, which greatly improves the stability and convergence of the solution, and its expression is

$$\frac{\partial}{\partial t}(\rho_m) + \frac{\partial}{\partial x_i}\left(\rho_m u_{m,j}\right) = 0 \tag{17}$$

$$\frac{\partial}{\partial t}(\rho_m u_{m,i}) + \frac{\partial}{\partial x_j}(\rho_m u_{m,i} u_{m,j}) = -\frac{\partial p}{\partial x_i} + \frac{\partial}{\partial x_j}\left[\mu_m\left(\frac{\partial u_{m,i}}{\partial x_j} + \frac{\partial u_{m,j}}{\partial x_i}\right)\right] + \rho_m g_i + \sum_{p=1}^{n} \alpha_p \rho_p u_{dr,pi} u_{dr,pj} + F_i \quad (18)$$

In the formula, ρ_m, u_m, and μ_m are the density, velocity, and viscosity of the mixed phase, respectively, which can be obtained by weighting the volume fraction of each phase. The interphase motion difference is calculated by the slip velocity $u_{dr,pi}$ which is expressed as

$$u_{dr,pi} = u_{pq,i} - \sum_{k=1}^{n} c_k u_{q,i} \quad (19)$$

In the above formula, $u_{pq,i}$ is the relative velocity between the p phase and the main phase (q phase), c_k is the mass fraction of the k phase, and $u_{qk,i}$ is the relative velocity between the q phase and the k phase.

The basic assumption of the ASM is that each phase can reach local equilibrium on a small spatial scale, that is, the particles can be accelerated to their respective local terminal velocity of particle settling in a short time, therefore, the particle size cannot be too large. According to the Manninen formula [28], the relative velocity $u_{pq,i}$ is defined as:

$$u_{pq,i} = \frac{\tau_p}{f_\mathrm{d}} \frac{(\rho_p - \rho_m)}{\rho_p} a_i \quad (20)$$

where f_d is the drag function, and a_i is the acceleration in the i direction, which can be calculated by the following formula:

$$a_i = g_i - u_{mj} \frac{\partial u_{m,i}}{\partial x_j} - \frac{\partial u_{m,i}}{\partial t} \quad (21)$$

In order to consider the effect of turbulent flow on particle motion, the turbulent diffusion force needs to be added to Equation (20), so as to obtain:

$$u_{pq,i} = \frac{\tau_p}{f_{drag}} \frac{(\rho_p - \rho_m)}{\rho_p} a_i - \frac{\eta_t}{\sigma_t}\left(\frac{1}{\alpha_p}\frac{\partial \alpha_p}{\partial x_i} - \frac{1}{\alpha_q}\frac{\partial \alpha_q}{\partial x_j}\right) \quad (22)$$

where η_t is the turbulent dissipation rate, σ_t is the Prandtl–Schmidt number, set to 0.75.

In addition to solving the mixed-phase differential governing equations, the scalar transport equations need to be solved for the volume fractions of each phase:

$$\frac{\partial}{\partial t}(\alpha_p \rho_p) + \frac{\partial}{\partial x_i}(\alpha_p \rho_p u_m) = -\frac{\partial}{\partial x_i}\left(\alpha_p \rho_p u_{dr,pi}\right) \quad (23)$$

Among them, the main phase volume fraction is not directly solved, but calculated by the following formula:

$$\alpha_q = 1 - \sum_{k=2}^{n} \alpha_p \quad (24)$$

In addition, when there are only two phases of gas and liquid in the system, the ASM and TFM can also be used to capture the gas–liquid interface when the particle diameter of the gas phase is small ($<10^{-5}$ m), but the interface accuracy is far lower than the VOF model [29].

In this paper, the simulation strategy shown in Figure 1 is used to study the flow field characteristics, separation performance, and particle movement behavior of hydrocyclones in two steps [30]. In the first step, the RSM-VOF or LES-VOF is used to simulate the gas–liquid two-phase flow field of the hydrocyclone, focusing on the analysis of the spatial distribution of the AVWZ and its internal flow field characteristics. In the second step, several particle phases are added, and the RSM-TFM or RSM-ASM is used to examine the separation performance of the hydrocyclone and the distribution of particles in the AVWZ with the basis of a stable gas–liquid two-phase flow field.

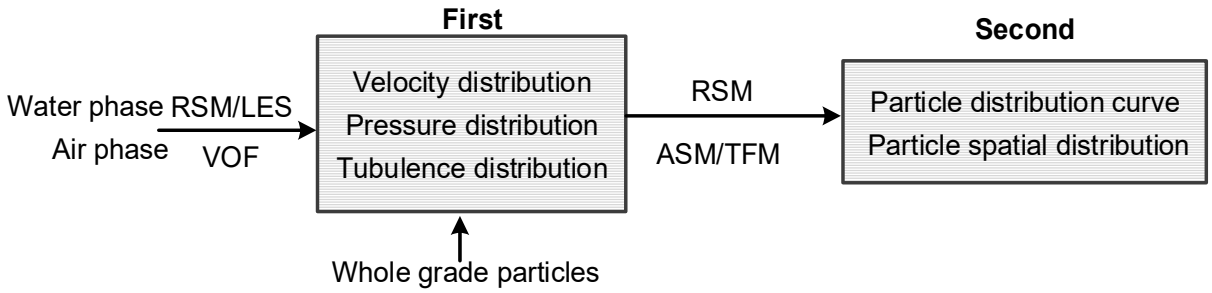

Figure 1. Modelling strategy for numerical tests.

2.2. Simulation Conditions and Boundary Conditions

The laboratory Φ150 mm hydrocyclone is mainly used to test the separation performance. Its geometric parameters and computational mesh are shown in Figure 2.

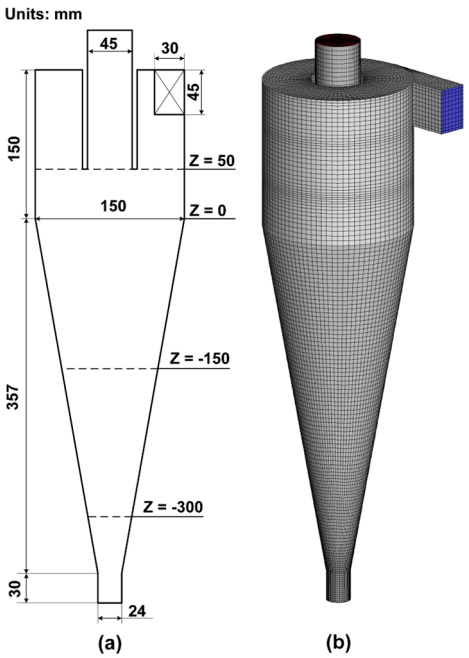

Figure 2. Schematic diagram of laboratory Φ150 mm hydrocyclone. (**a**) Geometrical parameters; (**b**) Computational mesh.

The grid independence check adopts three different grid schemes (170 k, 400 k, and 810 k cells). At the same time, the tangential velocity and the axial velocity at the axial position Z = 0 mm are used as the standard, and the results are show in Figure 3. As can be seen from Figure 2, when the number of cells exceeds 400 k, continuing to reduce the grid size has almost no effect on the calculation results. Therefore, when the RSM-VOF is adopted, the number of cells of the Φ150 mm hydrocyclone is 400 k. When the LES-VOF is adopted and the grid needs to be further refined, the third grid scheme is adopted and the number of cells is 810 k. When the structural parameters of the hydrocyclone change, the meshing method and the value range of Y+ of the wall remain unchanged, and only the meshes whose structure has changed need to be adjusted accordingly.

The initial conditions are mainly responsible for setting the flow field properties of the hydrocyclone at the initial moment. Although the initial conditions do not affect the final results of the numerical experiments, they can greatly affect the convergence speed of the calculations and the time it takes for the flow field to stabilize. In this paper, when the VOF model is adopted, the entire computational domain is filled with air and the velocity is zero at the initial moment.

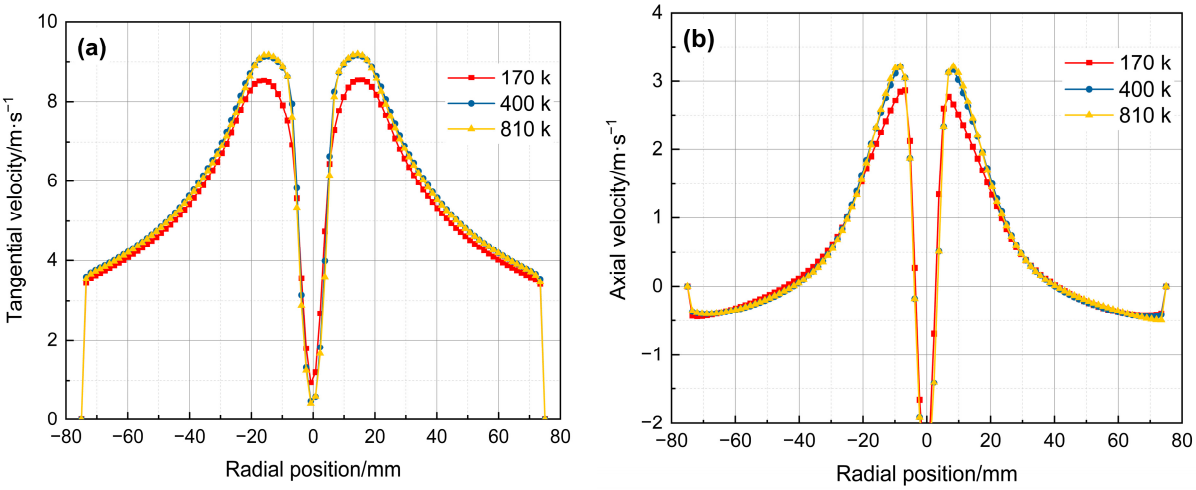

Figure 3. Grid independence test on laboratory Φ150 mm hydrocyclone. (**a**) Tangential velocity; (**b**) Axial velocity.

When the hydrocyclone works at a standard atmospheric pressure, the inlet type is usually set to velocity-inlet or flow-inlet, the outlet type is set to pressure-outlet, the wall type is set to non-slip wall, and the standard wall function is coupled to solve. Assuming fully developed turbulence at the inlet, the turbulence intensity (I) can be calculated from:

$$I = 0.16(\mathrm{Re_{in}})^{-1/8} \tag{25}$$

In this formula, $\mathrm{Re_{in}}$ is the inlet Reynolds number. The turbulence intensity of the vortex finder and spigot is usually set to 5% [31]. In addition, the coefficients of the recirculation of air at the outlet are all set to 1 to ensure the formation of air core.

The boundary conditions of the laboratory Φ150 mm hydrocyclone are shown in Table 1. These options in Table 1 are all set in ANSYS Fluent (18.0, Ansys, Pittsburgh, PA, USA). ANSYS Fluent is the world's leading general-purpose computational fluid dynamics (CFD) commercial software, which uses CFD numerical simulation technology to provide solutions to fluid problems for engineers in various industries around the world. It is a widely used and powerful commercial CFD software in the world today.

Table 1. Boundary conditions of laboratory Φ150 mm hydrocyclone.

Boundary	Type	Pressure (kPa)	Phase	Velocity (m/s)	Turbulence Intensity (%)	Volume Fraction (%)
inlet	velocity-inlet	Cal.	air water limestone	3.70 3.70 3.70	3.66	0.00 80.00–100.00 0.00–20.00
overflow underflow	pressure-outlet	101.00	air water limestone	Cal. Cal. Cal.	5.00	Cal. Cal. Cal.
	pressure-outlet	101.00	air water limestone	Cal. Cal. Cal.	5.00	Cal. Cal. Cal.

2.3. Solving Conditions and Model Validation

2.3.1. Solving Conditions

In this paper, the finite volume method is used to discretize and solve the differential governing equations, which can ensure the conservation of physical quantities in the discretization process. In the process of solving the momentum conservation equation, due to the lack of a corresponding equation for the pressure term, the coupled solution of the pressure field and the velocity field needs to be calculated iteratively by means of prediction

and correction. This paper mainly adopts SIMPLE (Semi-Implicit Method for Pressure-Linked Equations) proposed by Patankar and Spalding [32] to solve pressure-velocity field coupling. The PRESTO interpolation method is selected for pressure solutions, and the QUICK scheme is used for the transport equations of momentum, dispersed phase, and turbulence. In addition, the residuals of all terms in the differential governing equations are limited below 10-4 to guarantee the solution accuracy. When the RSM turbulence model is adopted, the time step is 5×10^{-4}~10^{-3} s; when the LES turbulence model is adopted, the time step is 5×10^{-5} s to improve the capture accuracy of large eddies by the LES. When the numerical test results are statistically stable, continue to calculate for 3 s for sampling average, and use it as the final simulation result.

2.3.2. Comparison and Validation of Two-Phase Flow Models

The comparison and verification of the two-phase flow model are based on a Φ75 mm hydrocyclone, and RSM is used to simulate turbulent flow [33]. The VOF model assumes that gas and liquid are incompatible with each other, and the gas–liquid interface can be accurately captured using the Geo-reconstruct format. The ASM assumes that the gas and liquid phases are an interpenetrable continuum, and even without considering the slip velocity between the phases, the dispersed gas–liquid interface can only be captured by the QUICK format. In order to examine the changes in the gas–liquid interface when switching from the VOF model to the ASM, Figure 4 compares the changes in the axial diameter of the air column obtained by VOF, ASM, and LDA. The results show that the air column predicted by the VOF model is basically consistent with the LDA measurement result, and the diameter of the air column is about 10 mm. When the ASM is used, the contour lines when the air volume fraction α_{air} is 0.1 and 0.9 are taken as the upper and lower limits of the air column boundary. When α_{air} = 0.1, the diameter of the air column predicted by the ASM is about 15 mm, which is much larger than the measured value of LDA; when α_{air} = 0.9, the diameter of the air column predicted by the ASM is about 9 mm, slightly smaller than the measured value of LDA. On the one hand, this shows that the gas–liquid interface obtained by the ASM is very dispersed; on the other hand, the range of the gas–liquid interface predicted by the ASM includes the LDA measurements, indicating that the model can also accurately simulate the gas–liquid two-phase flow field.

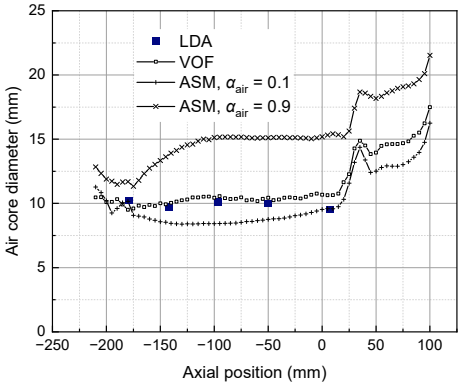

Figure 4. Comparison of air core diameters obtained from numerical tests and LDA measurements.

2.3.3. Comparison and Validation of Multiphase Flow Models

The comparison and verification of multiphase flow models are mainly based on Φ75 mm and Φ150 mm hydrocyclones, and the ASM are examined.

Model Verification of Φ75 mm Hydrocyclone

The test process and separation results of the Φ75 mm hydrocyclone refer to Hsieh's research [34]. In order to fully examine the reliability of the multiphase flow model, the overflow products, underflow products, and recovery to underflow obtained from

numerical tests and physical tests were compared, respectively. The results are shown in Figures 5 and 6, respectively.

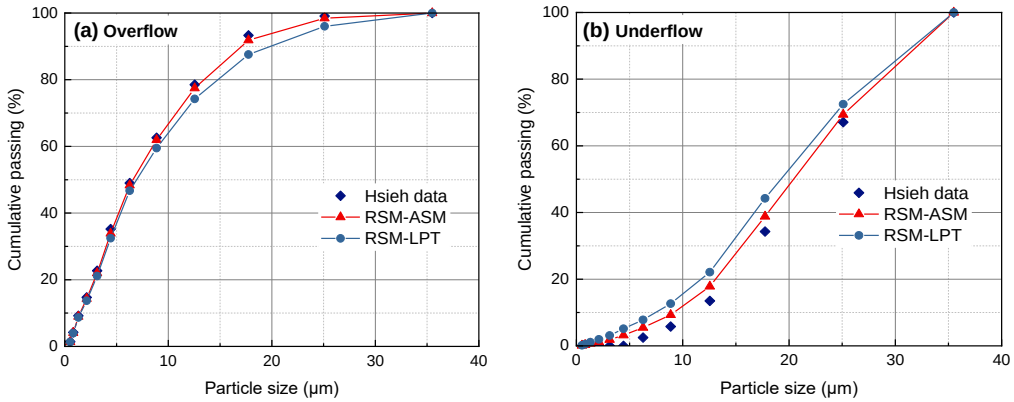

Figure 5. Comparison of particle size distribution in products of the Φ75 mm hydrocyclone. (**a**)—Overflow product; (**b**)—Underflow product.

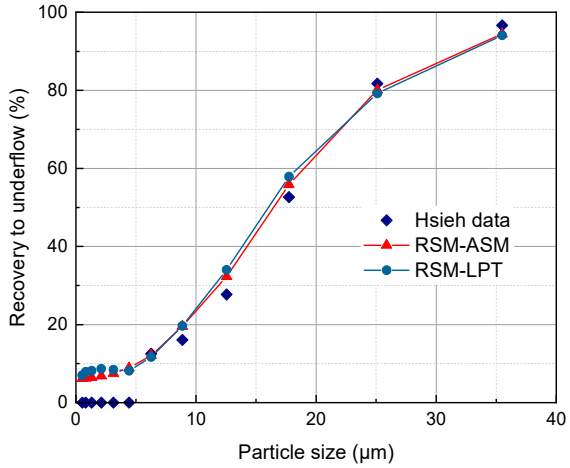

Figure 6. Comparison of partition curves of the Φ75 mm hydrocyclone.

The results in Figure 5 show that the ASM can better predict the particle size composition of the overflow product and the underflow product, but slightly overestimates the content of fine particles in the underflow, while the prediction results of the LPT (Lagrange Particle Tracking) model have a certain deviation from the test results. The reasons for this are largely due to the following two points: (1) The RSM-ASM underestimates the pressure distribution in the hydrocyclone, which leads to an increase in the recovery to underflow and an increase in the content of fine particles; (2) Although the LPT model is based on the ASM, it only acts on the main phase (water), and does not fully consider the influence of other particles on the tracking particles.

The results in Figure 6 show that the simulation results of the ASM are in good agreement with the physical test results, but there is a certain deviation in the prediction of the distribution rate (or separation efficiency) of fine particles. Theoretically, the fine particles have strong followability, and usually have a recovery to underflow similar to the water flow ratio. In Hsieh's test, the water split ratio was 4.32%, and the recovery to underflow of particles smaller than 5 μm was basically zero, which may be caused by sampling error and laser particle size detection error [35]. The distribution rate of fine particle underflow predicted by the ASM is close to the water flow ratio, indicating that the numerical test model can accurately predict the separation performance of the hydrocyclone. In addition, LPT can also more accurately predict the change trend in separation particle size and sand distribution curve. To summarize, under the condition of

lower ore feeding concentrations, the prediction accuracy of the ASM and LPT model are both acceptable.

Model Verification of Φ150 mm Hydrocyclone

The schematic diagram of the laboratory Φ150 mm hydrocyclone classification system and the experiment device are shown in Figure 7. It can be seen from Figure 7, the laboratory Φ150 mm hydrocyclone classification platform is mainly composed of four parts: the measurement and control system that the different colors of the control system represent start and stop buttons and instruments the feeding system, the classification system, and the sampling system, which is convenient for quickly and accurately adjusting working conditions and obtaining experiment data. Among them, the measurement and control system includes an electromagnetic flowmeter, a pressure sensor, and a control cabinet for displaying measurement data and adjusting the frequency of the motor. During the experiment, the agitaton intensity and the rotational speed of the centrifugal pump can be adjusted through the control cabinet to achieve uniform and stable feeding. The sampling system is composed of a grit chamber, an overflow box, and a bypass pipeline. During the experiment, samples can be taken from the bypass pipe, the lower part of the grit chamber, and the outlet of the overflow box at the same time to ensure the accuracy of the test data.

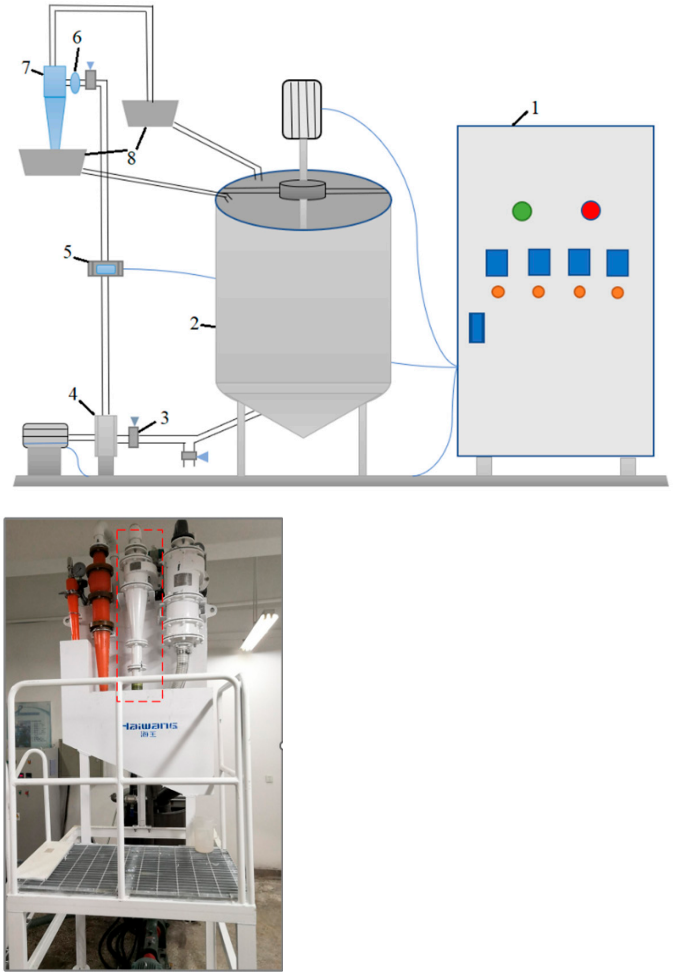

Figure 7. Schematic diagram and implementation of laboratory test rig on the Φ150 mm hydrocyclone. 1—Electric cabinet; 2—Mixing tank; 3—Butterfly valves; 4—Centrifugal pump; 5—Magnetic flowmeter; 6—Pressure transmitter; 7—Hydrocyclone; 8—Product sumps.

The simple test procedure is as follows. Under the set feed concentration, add the corresponding quality of quartz sample and water into the mixing tank. After fully stirring,

drive the material into the separation system under relatively high pressure. After the system is stabilized, obtain the feed, overflow, and underflow samples from the return pipe, vortex finder, and spigot, respectively, then weigh their wet and dry weights, and calculate the water yield, particle yield, and recovery to underflow.

In order to ensure the accuracy of the physical test, three repeated tests were carried out for each group of working conditions, and the final results were averaged. The results show that the composition of the feed particle size is relatively stable during the test, and the fluctuation of the yield of each particle grade is less than 2%. At the same time, the measured feed particle size distribution is basically consistent with the synthesized feed particle size distribution, and the error of each particle size yield is essentially within 3%, which shows the stability and reliability of the physical test results. Therefore, the above model is used to verify the reliability of this research content test.

In order to fully examine the reliability of the multiphase flow model, the separation results of the numerical test and the physical test of the Φ150 mm hydrocyclone at different feed concentrations are compared in Figure 8.

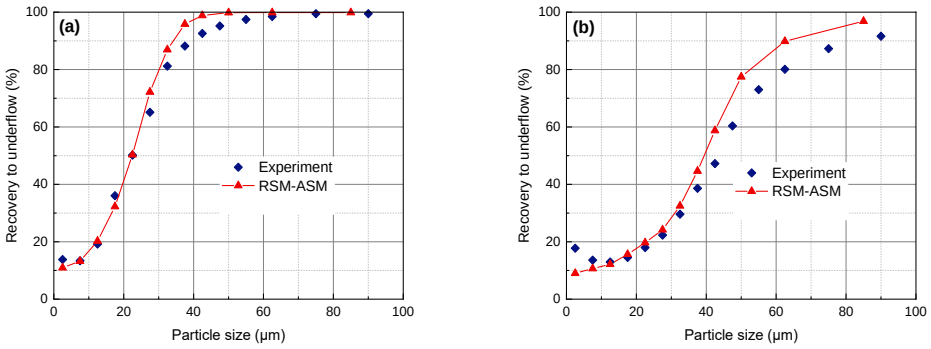

Figure 8. Comparison of partition curves of Φ150 mm hydrocyclone. (**a**)—Cv = 5%; (**b**)—Cv = 15%.

Figure 8 shows that at a lower feed concentration (Cv = 5%), the ASMs can all accurately predict the recovery to underflow and separation size, and the maximum error is less than 8%, but they all overestimate the recovery to underflow of the coarse particle size. When the Cv is 15%, the ASM does not consider the particle friction stress and friction viscosity, resulting in a higher recovery to underflow of coarser particles. This means particle interactions have a greater influence on separation results under the condition of a high concentration feed.

3. Results and Discussion

3.1. Effects on Separation Performance

The effects of the inlet diameter (D_i), the inlet and inlet aspect ratio (h/w), the inlet on the water split, and the recovery underflow are shown in Table 2.

Table 2. Effects of inlet structure on the water split and recovery underflow.

Parameters	D_i/D					h/w				
	0.22	**0.25**	**0.28**	**0.30**	**0.33**	**0.50**	**1.00**	**1.50**	**2.00**	**2.50**
R_w/%	4.77	5.68	6.90	9.25	12.58	8.62	7.26	6.90	6.67	6.54
γ_u/%	68.80	67.54	64.96	62.16	60.55	62.57	63.96	64.96	65.33	65.66

It can be seen from Table 2 that with the increase in the inlet diameter, the water split gradually increases, while the particle yield gradually decreases. With the increase of the inlet aspect ratio, the change trend is opposite.

According to the Figure 9a,b, the recovery underflow and the cut size of fine particles gradually increase with the increase in the inlet diameter, while the recovery underflow

of coarse particles gradually decreases. Correspondingly, the corrected cut size gradually increases, the Ecart probable E_p gradually increases, and the index α gradually decreases, indicating that the separation accuracy gradually decreases. With the increase in the inlet aspect ratio, the recovery underflow of fine particles decreases slightly, and the recovery underflow of coarse particles increases gradually. Meanwhile, the corrected cut size decreases rapidly and then decreases slowly, the E_p gradually decreases, and the index α also increases gradually, indicating that the separation accuracy is improved.

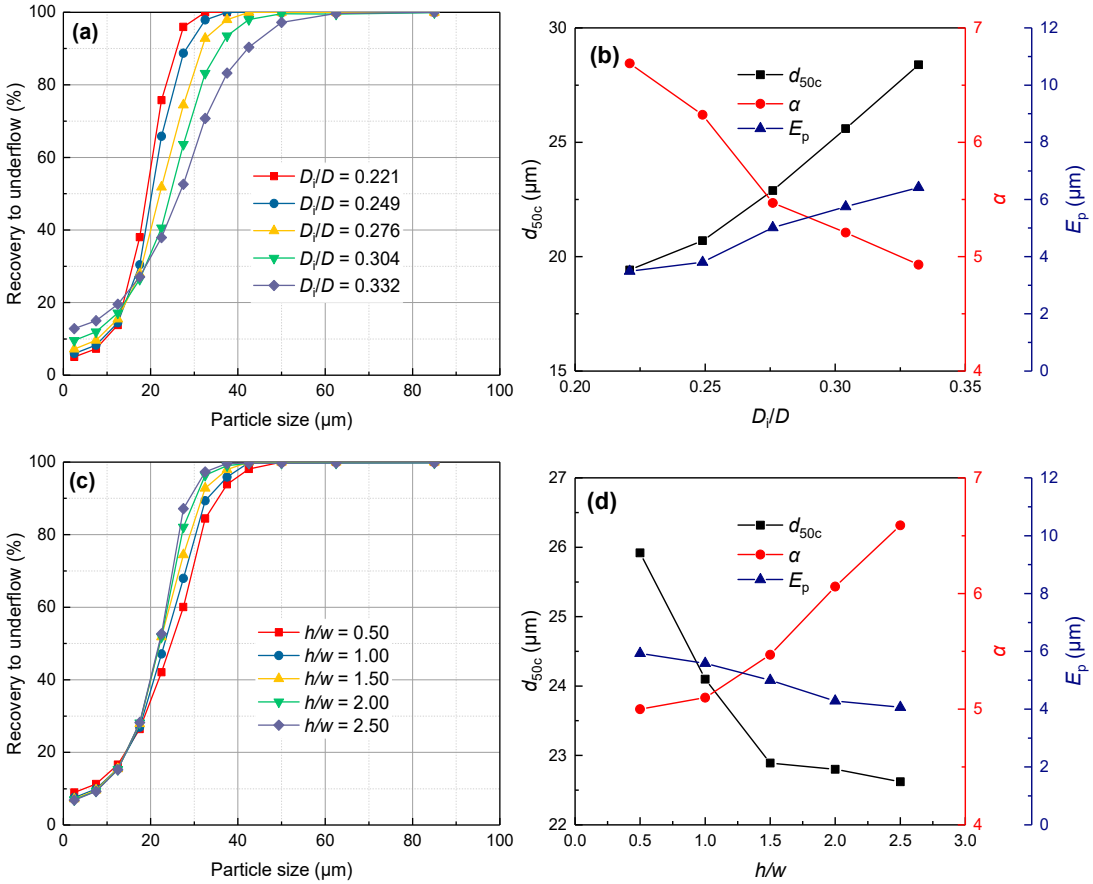

Figure 9. Effects of inlet structure on separation performance. (**a**,**b**)—D_i/D; (**c**,**d**)—h/w.

3.2. Effects on the Internal Flow Field in the AVWZ

3.2.1. Definition Method of AVWZ Based on RSM

According to the LDA test results, the axial velocity near the LZVV is small and varies slowly. Based on this, the AVWZ can be defined as the region where the average axial velocity $\overline{u_k}$ is less than the characteristic velocity v_c, and the expression is:

$$\dot{v} = |\overline{u_k}| - v_c \tag{26}$$

In the formula, $\dot{v}$ is the discriminant speed, and $\dot{v} < 0$ means that the point is inside the AVWZ.

Second, according to the RSM-VOF simulation results, although the axial velocity near the LZVV is small, the turbulence intensity is large. Based on this, the AVWZ can be defined as the region where the axial average velocity $\overline{u_k}$ is less than the axial pulsating velocity $\overline{u_k'}$, and the expression is:

$$\dot{v} = |\overline{u_k}| - \overline{u_k'} \tag{27}$$

Finally, according to the LES-VOF simulation results, the axial instantaneous velocity fluctuates wildly around zero velocity. Based on this, the AVWZ can be defined as all regions where the axial instantaneous velocity may be zero, and the expression is:

$$\dot{v} = |\overline{u_k}| - \left(u'_{k,\mathrm{rms}} + \overline{u'_{k,\mathrm{sgs}}}\right) \tag{28}$$

where $|\overline{u_k}|$ and $u'_{k,\mathrm{rms}}$ are the average velocity and fluctuating velocity, respectively. $\overline{u'_{k,\mathrm{sgs}}}$ is the subgrid pulsation calculated by the subgrid turbulence model speed. In fact, the second definition and the third definition are essentially the same, the fluctuation range of an instantaneous LZVV is the spatial distribution range of the AVWZ.

3.2.2. Effects on Pressure and Tangential Velocity Distributions

Effects on pressure and the tangential velocity distributions of the construction of the inlet is shown in the Figure 10.

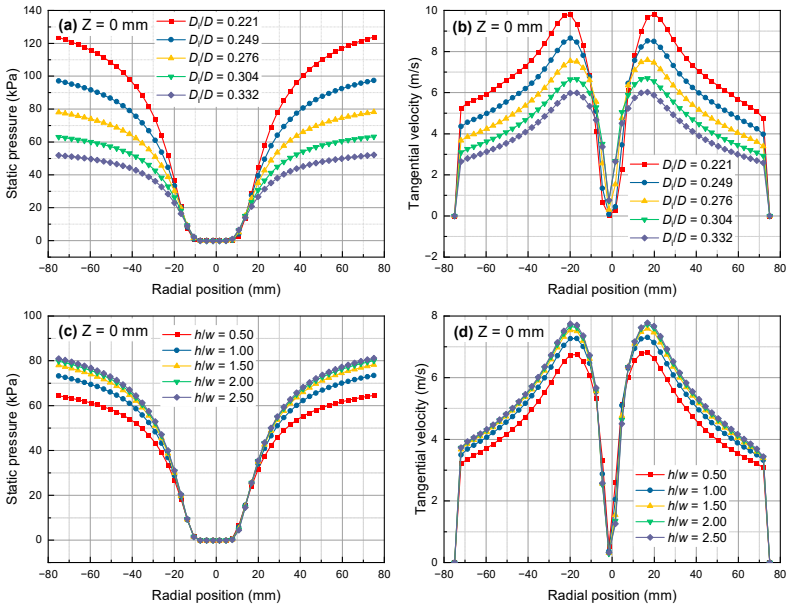

Figure 10. Effects of inlet structure on the distributions of pressure and tangential velocity (**a**,**b**)—D_i/D; (**c**,**d**)—h/w.

Figure 10a,b shows that in the case of a fixed feed flow, with the increase in the inlet diameter the velocity of the inlet gradually decreases, and the tangential velocity of the flow field inside the AVWZ also decreases, and subsequently the pressure also decreases accordingly. Correspondingly, the overall energy consumption of the hydrocyclone reduces, but the centrifugal strength is also weakened, therefore the separation accuracy decreases. In Figure 10c,d, both the internal pressure and the tangential velocity of the AVWZ decrease with the increase in the inlet aspect ratio, but the change range gradually becomes slower. Correspondingly, the overall energy consumption of the hydrocyclone increases, but the centrifugal inertia of the particles increases gradually, and the partition particle size gradually decreases.

3.2.3. Effects on Turbulence Intensity and Distribution of AVWZ

The effect of inlet structure on turbulence intensity and the AVWZ distribution is shown in Figure 11.

As shown in Figure 11a, with the increase in the inlet diameter, the turbulence intensity of the separation space gradually increases, especially in the lower part of the cone and inside the AVWZ. The spatial distribution range of the AVWZ also gradually expands, and the distribution range of the external swirling flow gradually decreases. As can be seen from Figure 11b, the inlet aspect ratio has little effect on the turbulence intensity and the AVWZ distribution of the entire separation space.

The effect of the inlet structure on the volume of the AVWZ and its proportion to the entire separation space is shown in Figure 12.

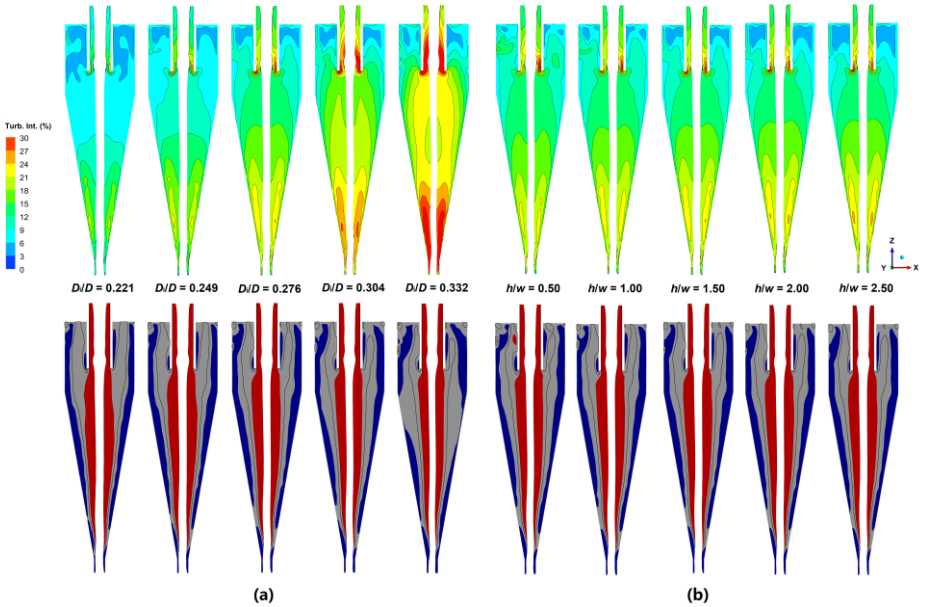

Figure 11. Effects of inlet structure on the distributions of turbulence intensity and AVWZ. (**a**)—D_i/D; (**b**)—h/w.

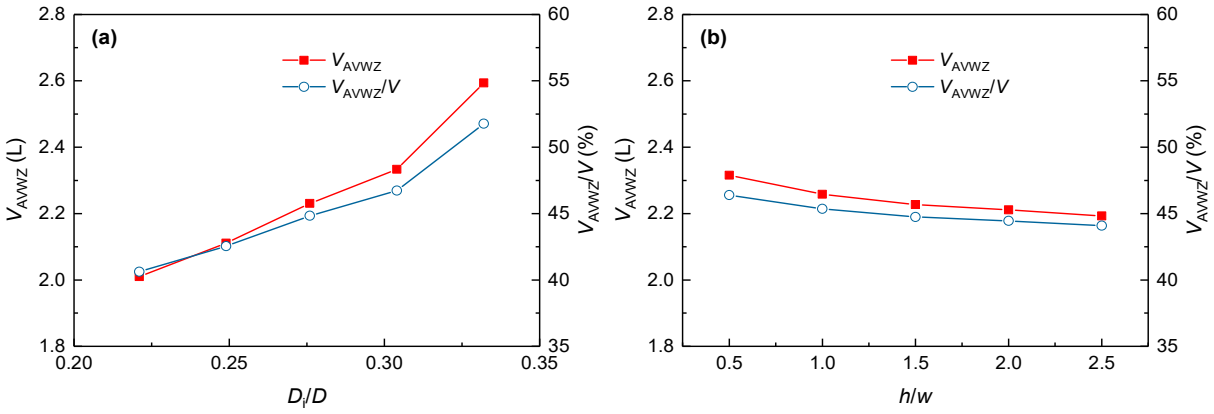

Figure 12. Effects of inlet structure on the AVWZ volume. (**a**)—D_i/D; (**b**)—h/w.

The results in Figure 12a show that with the increase in the inlet diameter, the volume of the AVWZ gradually increases, and its proportion in the entire separation space increases from 49% to 52%. According to the flow field characteristics of the AVWZ, the increase in its volume will inevitably lead to more particles entering the AVWZ, thereby reducing the separation accuracy. The results in Figure 12b show that the volume of the AVWZ and its proportion to the entire separation space decrease slowly with the increase in the aspect ratio of the entrance.

From the above results, the increase in the AVWZ range will lead to a decrease in separation performance, but the separation performance is not only related to the AVWZ range.

3.2.4. Effects on Particle Distribution Inside the AVWZ

The effect of the inlet on the equilibrium orbit radius of medium-sized particles is shown in Figure 13.

As shown in Figure 13, with the increase in the inlet diameter, the diameter of the air core gradually decreases, and the LZVV gradually moves to the axis, and the water split gradually increases. The inner side of the AVWZ gradually moves toward the axis, and the outer boundary gradually moves toward the wall, and the overall volume increases. The equilibrium gyration radius of medium-sized particles gradually moves closer to the

axis due to the decrease in centrifugal strength, and the variation range is larger than that of the inner boundary of the LZVV and AVWZ, resulting in more particles passing through the AVWZ and being discharged with the overflow, and subsequently the yield of sand particles reduces gradually. In addition, the spacing of the equilibrium gyration radius of particles with different strengths gradually decreases, and the separation accuracy gradually decreases. It can be seen from Figure 13b that with the increase in the inlet aspect ratio, the positions of the air column, the LZVV, and the AVWZ are basically unchanged, but the equilibrium gyration radius of medium-sized particles gradually moves closer to the wall. It can be seen that with the increase in the inlet aspect ratio, the centrifugal strength inside the AVWZ will increase, and the centrifugal inertial force on the particles at the same position will be larger. A larger inlet aspect ratio will reduce the distance between the particles in the feed channel and the wall, and medium-to-coarse particles can quickly settle to the wall. When the inlet structure is wider, the feed material will directly enter the AVWZ, resulting in an increase in the cut size and a decrease in the separation accuracy. Therefore, a reasonable feed body should be able to provide pre-separation or a small settling distance, and the turbulence intensity inside the cyclone, especially the axial velocity fluctuation, is low.

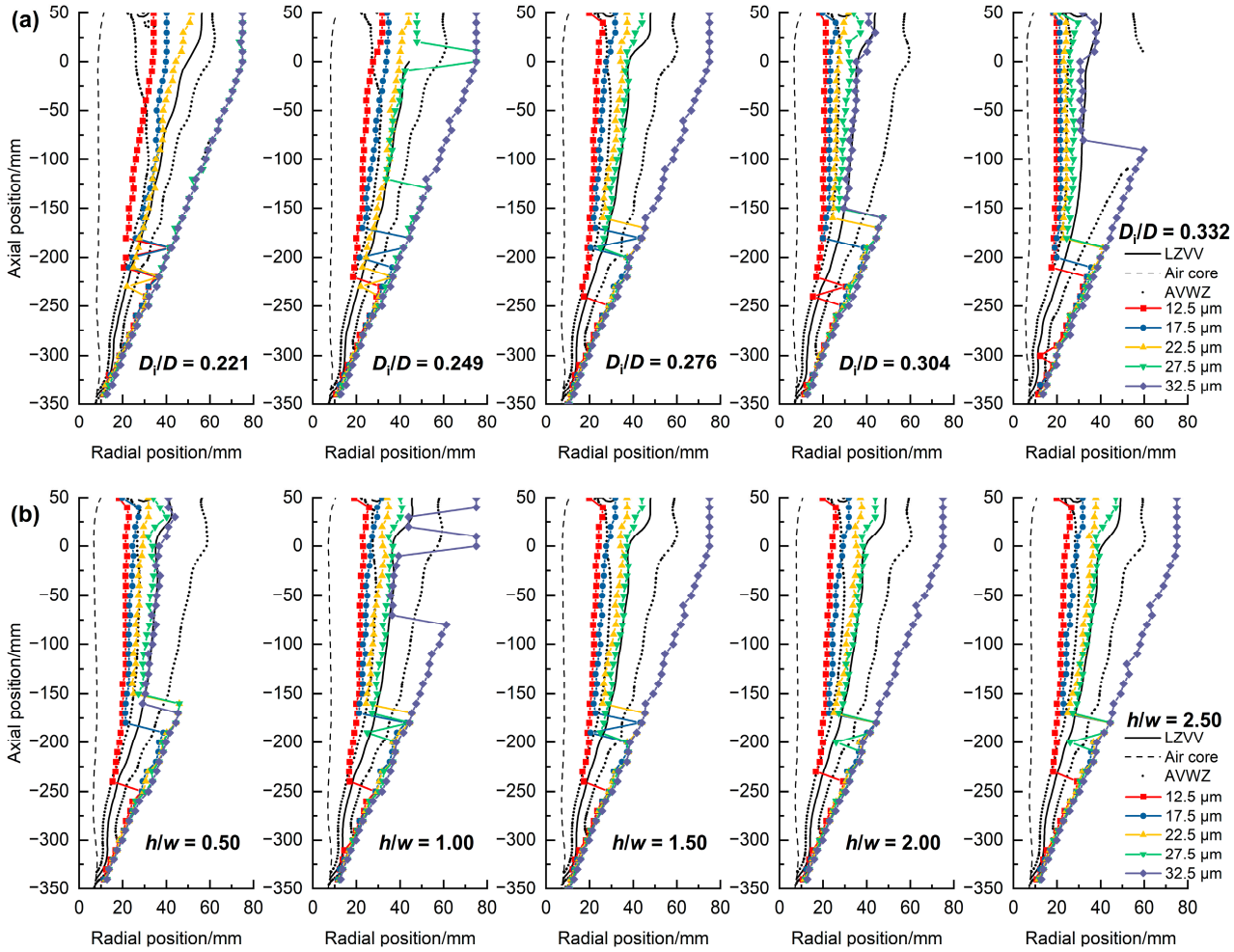

Figure 13. Effects of inlet structure on the equilibrium radius of intermediate-sized particles. (**a**)—D_i/D; (**b**)—h/w.

4. Conclusions

Based on the numerical test method, this paper analyzes the influence of the inlet structure on the internal flow field and particle distribution characteristics of the AVWZ and its internal relationship with the separation performance.

(1) The RSM-ASM model combined with the KTGF can be used to predict the separation performance of hydrocyclones under relatively low solid concentrations, and the error fluctuation between physical and numerical tests is largely less than 8%. Therefore, the influence rule of the inlet structure is consistent with the literature and has a good corresponding relationship with the AVWZ.
(2) Increasing the inlet diameter can decrease the pressure and tangential velocity of the fluid inside the AVWZ and the overall energy consumption of the hydrocyclone, but the centrifugal strength also decreases, meaning the cut size gradually increases. At the same time, the separation accuracy will decrease. This is mainly due to the fact that the inner boundary of the AVWZ is close to the air core, causing medium particles to pass through the AVWZ and be discharged with the overflow.
(3) Under the condition of a constant flow rate and a constant inlet cross-sectional area, with the increase in the height-to-width ratio of the inlet cross-section, the fluid pressure and tangential velocity in the AVWZ gradually increase. The range of AVWZ becomes larger, the composition of particles entering the AVWZ will increase, and the medium particles will quickly settle to the wall, correspondingly, the recovery to underflow gradually increases.
(4) According to the relationship between AVWZ and separation performance, controlling the range of AVWZ and the composition of particles entering the AVWZ will adjust the separation results. Under the same flow conditions, a smaller inlet and a larger height-to-width ratio are always beneficial to improve the separation accuracy, but the rapid energy consumption is also a matter of consideration.

Author Contributions: Conceptualization, Q.Z. and B.C.; methodology, Q.Z.; validation, Q.Z. and S.Z. (Shuo Zhang); investigation, Q.Z.; writing—original draft preparation, S.Z. (Shuo Zhang); writing—review and editing, B.C.; visualization, S.Z. (Shuo Zhang); supervision, S.Z. (Sikai Zhao) and Y.S. All authors have read and agreed to the published version of the manuscript.

Funding: This research received no external funding.

Acknowledgments: This work was financially supported by the National Key R&D Program of China [2021YFC2902700] and the National Natural Science Foundation of China [52174244, 52204265].

Conflicts of Interest: The authors declare no conflict of interest.

Nomenclature

C_V	feed concentration, %
u	velocity, m/s
g	Gravity, 9.18 m/s^2
F	body force, N
t	time, s
x_i	Cartesian coordinate
p	static pressure, Pa
Greek letters	
γ	particle yield, %
η	classification efficiency, %
α	air volume fraction, %
ρ	density, kg/m^3
μ	fluid viscosity, kg/(m·s)
φ_{ij}	pressure strain term
ε_{ij}	turbulent dissipation term
δ_{ij}	Kronecker delta
Subscripts	
u	underflow
t	tangential direction
k, p, q	phase k, p, q

References

1. Xu, J.L.; Luo, Q. *Flow Field Theory of Hydrocyclon*; Science Press: Beijing, China, 1998.
2. Chu, Y.L.; Chen, W.M.; Lee, X.Z. Effect of structural modification on hydrocyclone performance. *Sep. Purif. Technol.* **2000**, *21*, 71–86. [CrossRef]
3. Misiulia, D.; Andersson, A.G.; Lundström, T.S. Effects of the inlet angle on the flow pattern and pressure drop of a cyclone with helical-roof inlet. *Chem. Eng. Res. Des.* **2015**, *87*, 307–321. [CrossRef]
4. Luo, Q.; Deng, C.; Xu, J.; Lixin, Y.; Guangai, X. Comparison of the performance of water-sealed and commercial hydrocyclones. *Int. J. Miner. Process.* **1989**, *25*, 297–310.
5. Dai, G.Q.; Chen, W.M.; Li, J.M.; Chu, L. Experimental study of solid-liquid two-phase flow in a hydrocyclone. *Chem. Eng. J.* **1999**, *74*, 211–216. [CrossRef]
6. Liu, Y.; Yang, Q.; Qian, P.; Wang, H.-L. Experimental study of circulation flow in a light dispersion hydrocyclone. *Sep. Purif. Technol.* **2014**, *137*, 66–73. [CrossRef]
7. Renner, V.G. *The Action of the Hydrocyclone*; Imperial College London: London, UK, 1976.
8. Tarján, G. *Mineral Processing*; Akadémiai Kiadó: Budapest, Hungary, 1991.
9. Lilge, E.O. Hydrocyclone fundamentals. *Trans. Inst. Min. Metall.* **1962**, *71*, 285–337.
10. Babaoğlu, N.U.; Parvaz, F.; Hosseini, S.H.; Elsayed, K.; Ahmadi, A. Influence of the inlet cross-sectional shape on the performance of a multi-inlet gas cyclone. *Powder Technol.* **2021**, *384*, 82–99. [CrossRef]
11. Nenu, R.K.T.; Yoshida, H. Comparison of separation performance between single and two inlets hydrocyclones. *Adv Powder Technol.* **2009**, *20*, 195–202. [CrossRef]
12. Ishii, M.; Mishima, K. Two-fluid model and hydrodynamic constitutive relations. *Nucl. Eng. Des.* **1984**, *82*, 107–126. [CrossRef]
13. Zhang, C.E.; Wei, D.Z.; Cui, B.Y.; Li, T.S.; Luo, N. Effects of curvature radius on separation behaviors of the hydrocyclone with a tangent-circle inlet. *Powder Technol.* **2017**, *305*, 156–165. [CrossRef]
14. Chu, Y.L.; Chen, W.M. *A Theroy of Hydrocyclone Separation*; Metallurgical Industry Press: Beijing, China, 2002.
15. Gomez JA, D. Modeling of 75- and 250-mm Hydrocyclones and Exploration of Novel Designs Using Computational Fluid Dynamics. Ph.D. Thesis, The University of Utah, Salt Lake City, UT, USA, 2006.
16. Li, J.; Jiang, C.; Kuang, S.B.; Zheng, Q.; Chu, K.W.; Yu, A.B. Prediction of separation performance of hydrocyclones by a PC-based model. *Sep. Purif. Technol.* **2019**, *211*, 141–150.
17. Yang, Q.; Lv, W.J.; Liang, M.; Wang, H.L. CFD study on separation enhancement of mini-hydrocyclone by particulate arrangement. *Sep. Purif. Technol.* **2013**, *102*, 15–25. [CrossRef]
18. Delgadillo, J.A.; Rajamani, R.K. A comparative study of three turbulence-closure models for the hydrocyclone problem. *Int J Miner Process* **2005**, *77*, 217–230. [CrossRef]
19. Shur, M.L.; Spalart, P.R.; Strelets, M.K.; Travin, A.K. A hybrid RANS-LES approach with delayed-DES and wall-modelled LES capabilities. *Int. J. Heat Fluid Flow* **2008**, *29*, 1638–1649. [CrossRef]
20. Zhao, Q.; Cui, B.Y.; Wei, D.Z.; Feng, Y.Q.; He, Y.; Bayly, A.E. Linking separation sharpness with the characteristics of axial velocity wave zone in a hydrocyclone. *Powder Technol.* **2021**, *386*, 467–482. [CrossRef]
21. Cui, B.Y.; Zhang, C.E.; Zhao, Q.; Hou, D.X.; Wei, D.Z.; Song, T.; Feng, Y.Q. Study on interaction effects between the hydrocyclone feed flow rate and the feed size distribution. *Powder Technol.* **2020**, *366*, 617–628. [CrossRef]
22. Mangadoddy, N. *Improved Computational and Empirical Models of Hydrocyclones*; The University of Queensland: Brisbane, Australia, 2009.
23. Sripriya, R.; Kaulaskar, M.; Chakraborty, S.; Meikap, B. Studies on the performance of a hydrocyclone and modeling for flow characterization in presence and absence of air core. *Chem. Eng. Sci.* **2007**, *62*, 6391–6402. [CrossRef]
24. Ahmadi, G.; Ma, D. A thermodynamical formulation for dispersed multiphase turbulent flows—1: Basic theory. *Int. J. Multiph. Flow* **1990**, *16*, 323–340. [CrossRef]
25. Wang, B.; Yu, A.B. Numerical study of the gas–liquid–solid flow in hydrocyclones with different configuration of vortex finder. *Chem. Eng. J.* **2008**, *135*, 33–42. [CrossRef]
26. Colli, A.N.; Fornes, J.P.; Pérez, O.G.; Bisang, J.M. Evaluation of a modified hydrocyclone as electrochemical reactor for processing of two-phase (gas-liquid) systems. *Electrochim. Acta* **2019**, *309*, 219–227. [CrossRef]
27. Zhao, Q.; Hou, D.X.; Cui, B.Y.; Wei, D.Z.; Song, T.; Feng, Y.Q. Development of an integrated multichannel inlet for improved particle classification in hydrocyclones. *Adv. Powder Technol.* **2021**, *32*, 4546–4561. [CrossRef]
28. Manninen, M.; Taivassalo, V.; Kallio, S. *On the Mixture Model for Multiphase Flow*; VTT Technical Research Centre of Finland: Espoo, Finland, 1996.
29. Kuang, S.B.; Chu, K.W.; Yu, A.B.; Vince, A. Numerical study of liquid-gas-solid flow in classifying hydrocyclones: Effect of feed solids concentration. *Miner. Eng.* **2012**, *31*, 17–31. [CrossRef]
30. Cui, B.Y.; Wei, D.Z.; Gao, S.L.; Liu, W.G.; Feng, Y.Q. Numerical and experimental studies of flow field in hydrocyclone with air core. *Trans. Nonferrous Met. Soc. China* **2014**, *24*, 2642–2649. [CrossRef]
31. Zhao, Q.; Cui, B.Y.; Wei, D.Z.; Song, T.; Feng, Y.Q. Numerical analysis of the flow field and separation performance in hydrocyclones with different vortex finder wall thickness. *Powder Technol.* **2019**, *345*, 478–491. [CrossRef]
32. Patankar, S.V. *Numerical Heat Transfer and Fluid Flow*; CRC Press: Boca Raton, FL, USA, 1980.

33. Hou, D.X.; Zhao, Q.; Cui, B.Y.; Wei, D.Z.; Song, Z.G.; Feng, Y.Q. Geometrical configuration of hydrocyclone for improving the separation performance. *Adv. Powder Technol.* **2022**, *33*, 103419. [CrossRef]
34. Hsieh, K.T. *Phenomenological Model of the Hydrocyclone*; University of Utah: Salt Lake City, UT, USA, 1988.
35. Cui, B.Y.; Zhang, C.E.; Wei, D.Z.; Lu, S.S.; Feng, Y.Q. Effects of feed size distribution on separation performance of hydrocyclones with different vortex finder diameters. *Powder Technol.* **2017**, *322*, 114–123. [CrossRef]